Supplementary Information

Gradient migration hydrogenation of adsorbed hydrogen modulated by asymmetric configuration of S vacancy with atomic Zn dopant for photocatalytic CO$_2$ methanation

Hao Shen,[a] Hang Gao,[a] Shuqu Zhang,*[a] Xia Liu,*[b] Lixia Yang,[a] Ren-Jie Song,[a] Jian-Ping Zou,[a] Shenglian Luo[a]

[a] Key Laboratory of Jiangxi Province for Persistent Pollutants Prevention Control and Resource Reuse, Nanchang Hangkong University, Nanchang 330063, Jiangxi Province, People's Republic of China

[b] College of Chemistry and Chemical Engineering, Qingdao University, Qingdao 266071, Shandong Province, People's Republic of China

*Corresponding authors:

Email address: zhangshuqu2013@126.com (S. Zhang); Liux918@163.com (X. Liu)

Contents

Experimental Section

Materials and reagents. Indium (III) chloride tetrahydrate ($InCl_3 \cdot 4H_2O$), thioacetamide (TAA), Zinc chloride ($ZnCl_2$) and Ethylene glycol (EG) were obtained from Shanghai Macklin Biochemical Technology Co, Ltd. (China). All chemical reagents were used without further purified in the experiments.

Synthesis of In_2S_3 and $xZn-In_{2-x}S_3$ (x=1%~6%). To synthesize In_2S_3 by a simple solvothermal method, 2 mmol of $InCl_3 \cdot 4H_2O$, and 3 mmol of TAA were dissolved in 30 mL of EG with continuous stirring for 2 h. Then, the mixture was maintained at 220 °C for 24 h in a 50 mL Teflon-lined autoclave. The orange precipitate was washed by deionized water and ethanol for several times after cooling down to room temperature. Finally, the obtained powders were collected by centrifugation, washed with deionized water and ethanol for several times, and freeze-dried for 12 h. The synthesis method of $xZn-In_{2-x}S_3$ is as same as In_2S_3 expect for $ZnCl_2$ addition (the molar ratios of Zn/(Zn + In) were 1, 2, 3, 4, 5, and 6%, and the total number of moles of (Zn + In) was 2 mmol, respectively).

Characterizations. The morphologies and the element mappings were obtained from a scanning electron microscopy (SEM, ZEISS Sigma 300, Germany). The morphologies and lattice fringes were obtained from a transmission electron microscopy (TEM, JEOL, JEM-2100 F, Japan) with an accelerating voltage of 200 kV. HAADF-STEM images were obtained from a FEI Titan cubed Themis G2 300 TEM/STEM with anaspherical aberration corrector. The crystalline phases composition was characterized by X-ray diffraction (XRD, Bruker D8 Advance, Germany) with Cu K α (λ = 1.542 Å). The electronic structures and chemical states of elements were analysis by X-ray photoelectron spectroscopy (XPS, Shimadzu KRATOS AXIS SUPRA +, Japan) with an exciting source of Al K α (0.1 eV). The extended X-ray absorption fine structure (EXAFS) and X-ray absorption near-edge spectra (XANES) were measured at Sci-go Research Service. The BL14W Beam line at the Shanghai Synchrotron Radiation Facility (SSRF) (Shanghai, China). The EPR measurements

were performed at room temperature using a spectrometer (Bruker, A-300) at 300 K and 9.86 GHz. The BET adsorption and desorption isotherms, pore size distribution was performed on a Belsorp-Mini II analyzer (Japan). The photoluminescence (PL) spectra were obtained and excited at 295 nm by a fluorescence spectrophotometer (Hitachi F4500, Japan) at room temperature. The time-resolved fluorescence spectrofluorometer (TRPL, Edinburgh FS5, Britain) with 320 nm excited wavelength was used to record the fluorescence emission spectra. An integrating sphere-equipped UV–*vis* spectrophotometer (DRS, Cary 300, America) was used to capture the diffuse reflection spectra (DRS) in the UV-*vis* range. The photocurrent response was tested in Na_2SO_4 aqueous solution (0.2 M, pH = 6.8) using an electrochemical workstation (Chenhua Instrument Co., Shanghai, China) with a three-electrode electrochemical system that Ag/AgCl electrode, Pt electrode, and fluoride tin oxide (FTO) with covered as-prepared photocatalysts (active area of 1.0×1.0 cm^2) were used as the reference electrode, counter electrode, and working electrode, respectively. The preparation process of the working electrode 20 mg photocatalysts were dispersed in 200 μL of ethyl alcohol and 30 μL of Nafion to obtain a suspension after ultrasonic treatment, then coated onto FTO glass substrate uniformly. After that, the coated FTO glass was dried at 60 °C. The transient photocurrent response was also evaluated under visible-light irradiation (the interval is 50 s for light on and off) at a fixed potential of 0.4 V *(vs.* Ag/AgCl) for 350s. The intermediate products for CO_2 adsorption and reduction were analyzed from *in-situ* Fourier transform infrared spectroscopy (Bruker INVENIO R, Germany). Photothermal mapping images were taken with a thermal infrared imager (FLIR E95−14). The isotope-labeled experiments were performed using D_2O instead of H_2O, and the products were analyzed using gas chromatography–mass spectrometry (Agilent 7890A AMETEK DAC 200 MS).

Performance evaluation for photocatalytic CO_2 reduction. 300 W Xenon lamp (Microsolar 300, Beijing China Education Au-light Co., Ltd.) was equipped with a 420 nm cutoff wavelength filter as a light source that simulates visible light for photocatalytic CO_2 reduction tests. The performance evaluation of photocatalytic CO_2 reduction was proceeded in a 50 mL quartz tube at atmospheric pressure and ambient

temperature. First, 2 mg of photocatalyst and 6 mL of water were added to a 50 mL quartz tube and sonicated for 1 min to disperse the catalyst; the quartz tube was then purged with high-purity CO_2 gas (99.999%) for 30 mins to completely remove air and injected with 1.0 atm of pure CO_2 (argon pressurization experiments continue to be performed on top of this by passing 0.1~0.8 atm argon gas); finally, the quartz tube is closed with a rubber stopper and sealing film. The reactor was placed under a Xenon lamp for photocatalytic reaction, and the current was 15 A. After reaction, the generated products (CH_4, CO and O_2) were analyzed qualitatively and quantitively by gas chromatograph (FL GC9790II, Zhejiang, China) equipped with flame ionization detector (FID) and thermal conductivity detector (TCD), while ultrahigh-purity argon was used as a carrier gas. The product was qualitatively and quantitatively analyzed by gas chromatography retention time and appearance standard curve method.

Calculation details. All calculations were performed by using the VASP package. The Perdew-Burke-Ernzerhof (PBE) within generalized gradient approximation (GGA) treats exchange-correlation functional, while projected augmented wave (PAW) describes the electron-io interaction. Grimme's zero-damping DFT-D_3 method was used to calculate van der Waals correction. For the plane-wave basis set, a cutoff of E_{cut} = 500 eV has been used. For bulk In_2S_3, Supercells consisting of 3×3×1 In_2S_3 unit cells were used and Brillouin zones were sampled using a Monkhorst−Pack k-point mesh with a 5×5×1 k-point grid. Meanwhile, the convergence criterion of energy and force within the process of geometric optimization is chosen as 10^{-5} eV and 0.01 eV/Å, respectively. A vacuum thickness of 15 angstroms were used to avoid virtual image interactions in all supercell models. The CI-NEB method and dimer method were used to determine transition state of reaction. The activation energy barrier E_a and reaction energy ΔE_r of reaction could be determined as $Ea = E_{TS} - E_{IS}$ and $\Delta E_r = E_{FS} - E_{IS}$ respectively, where E_{IS}, E_{FS} and E_{TS} are the energy of initial state, final state and transition state, respectively. Vibrational analyses were also carried out to verify transition states and local minimum. The CO_2 reduction reaction performance was evaluated by reaction free-energy change (ΔG) using spin-polarized calculation for each step, as shown in following equation:

$$\Delta G = \Delta E + \Delta E_{ZPE} - T\Delta S + \Delta G_{pH} + \Delta G_U$$

where ΔE is the difference between adsorption energies of a given group, ΔE_{ZPE} and ΔS are the differences in the zero-point energy and the change in entropy between adsorbed state and free-standing state, respectively; T is the temperature (T= 298.15 K), ΔG_U is the contribution of electrode potential (U) to shift free energy ΔG at applied U, and ΔG_{pH} is the correction of the H^+ free energy due to the influence of H^+ concentration ($\Delta G_{pH} = 2.303 \times k_B T \times pH \approx 0.059 \times pH$, where kB is Boltzmann constant and pH is assumed to be 0 in this work).
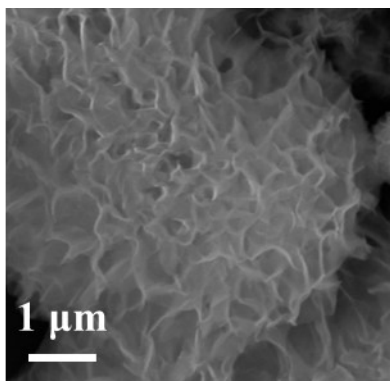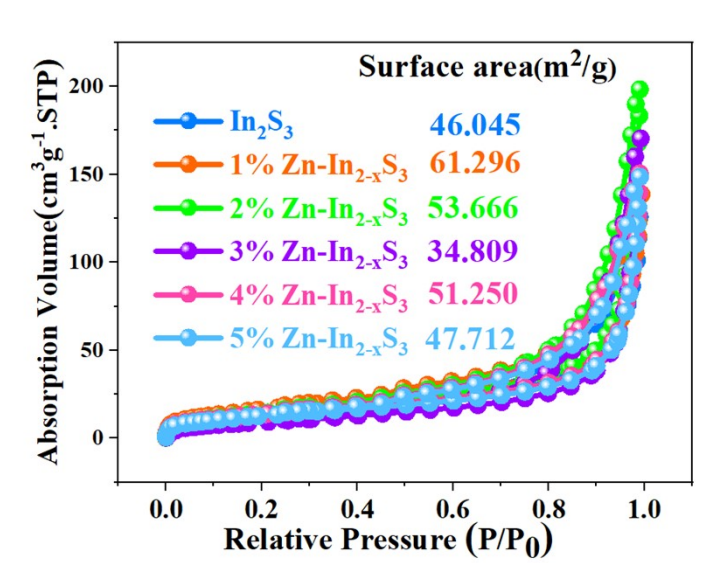
Supplementary Figures

Fig. S1 SEM image of In_2S_3.

Fig. S2 Nitrogen adsorption − desorption isotherms of In_2S_3 and $xZn−In_{2-x}S_3$ (x=1% ~ 5%).
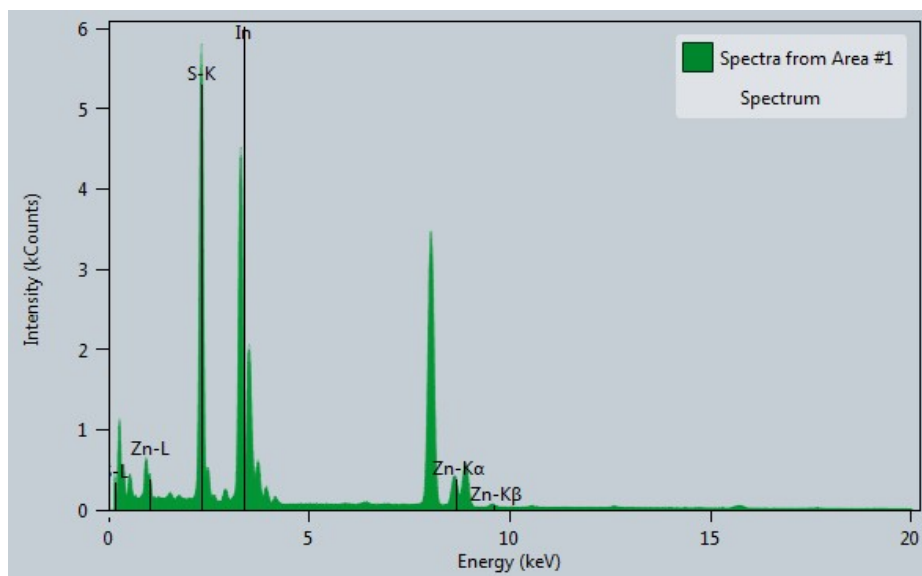
Fig. S3 EDS spectra of 4%Zn−In$_{2-x}$S$_3$.

Table S1. EDS results of 4%Zn−In$_2$S$_3$

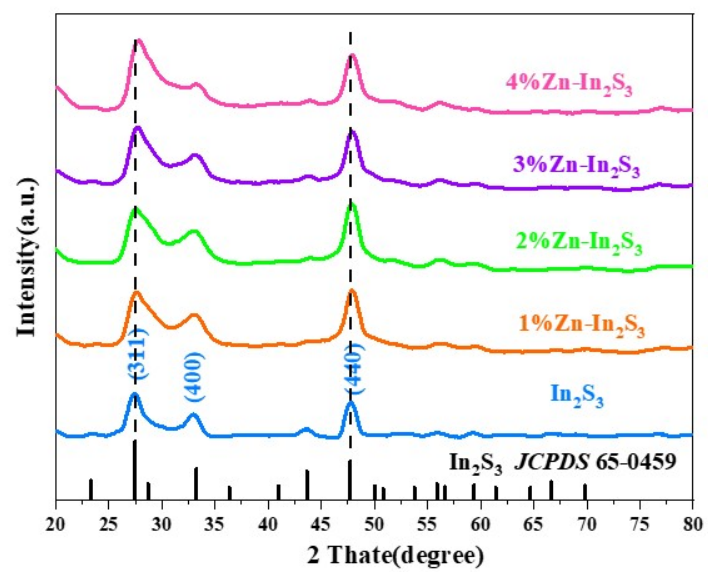| Element	Family	Atomic Fraction (%)	Mass Fraction (%)
S	K	58.55	29.55
In	L	35.74	64.58
Zn	K	5.71	5.87

Fig. S4 XRD pattern of In_2S_3 and $xZn-In_{2-x}S_3$ (x=1% ~ 4%).
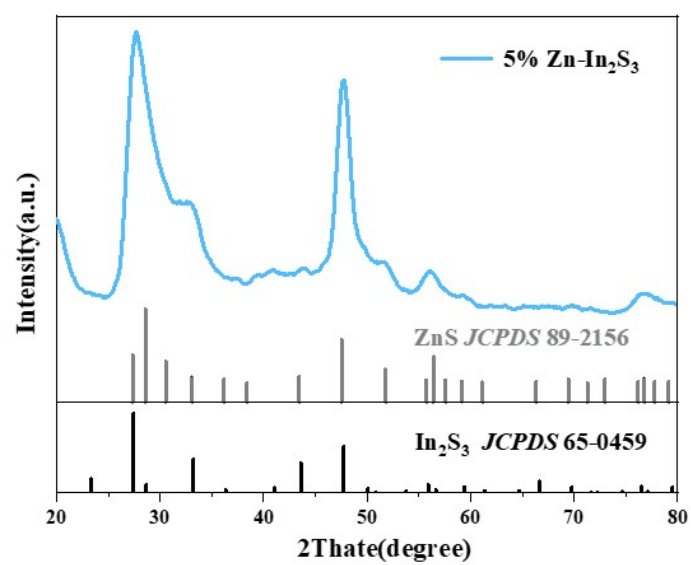
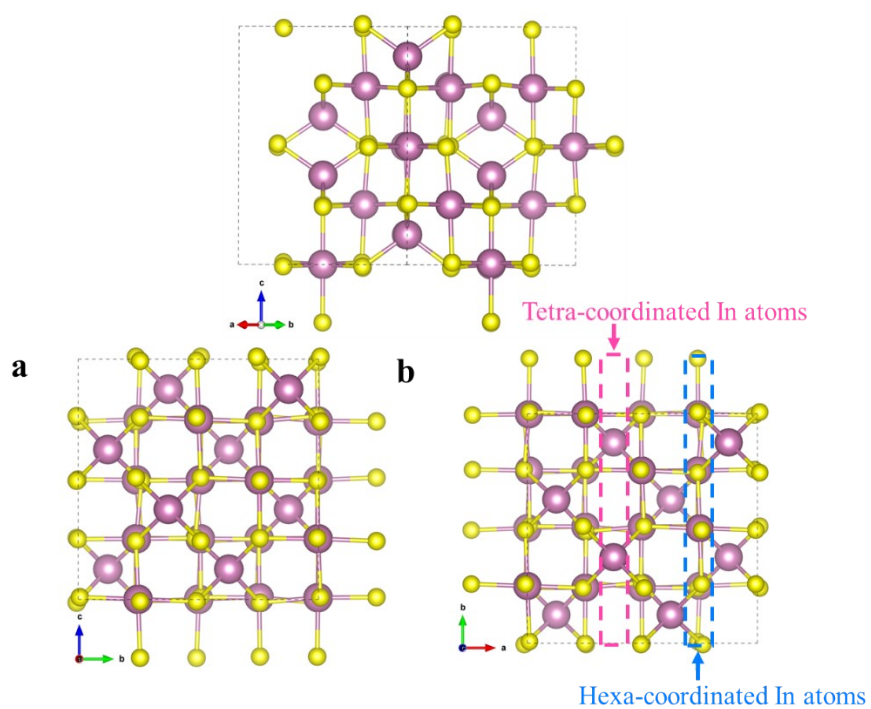**Fig. S5** XRD pattern of 5%Zn−In$_{2-x}$S$_3$.

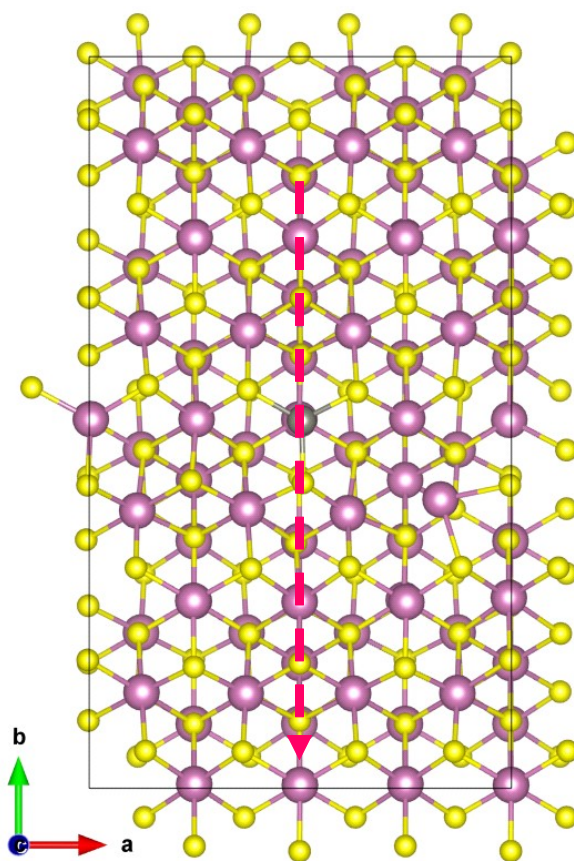**Fig. S6** Atomic modeling diagram of a single cell of bulk In_2S_3 : (a) front view. (b) top view.

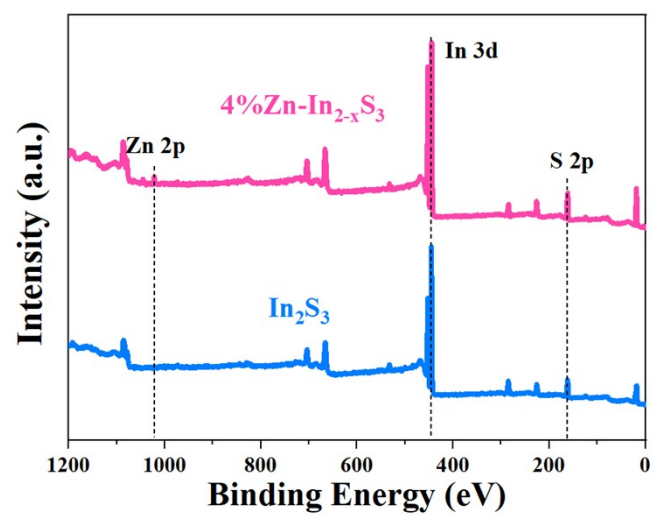**Fig. S7** Atomic model diagram for surface electrostatic potential over Zn-In$_{2-x}$S$_3$.

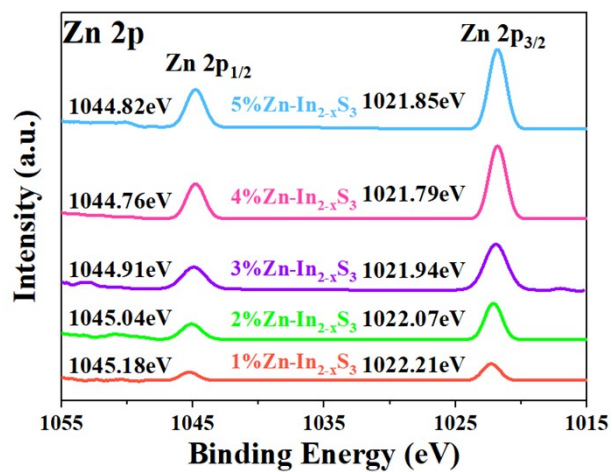**Fig. S8** XPS spectra of full spectrum for In_2S_3 and $4\%Zn-In_{2-x}S_3$.

Fig. S9 High resolution XPS spectra of Zn 2p over xZn−In$_{2-x}$S$_3$ (x =1% ~ 5%).

Table S2. XPS fitting data of area of elements, Zn atomic concentrations, the atomic ratios of S to In and V_S concentrations. The RSF (relative sensitivity factor) for Zn 2p, In 3d and S 2p are 5.589, 7.265 and 0.668 respectively.

Samples	Elements	Area/(T* MFP)	Area/(RSF *T*MFP)	Zn atom concentrations &	S: (In + Zn)*	Vs Concentrations[#]
In$_2$S$_3$	In 3d	112097.85	15429.8493	0.00%	1.49	0.81%
	S 2p	15335.1	22956.7365			
1%Zn−In$_2$$_{-x}S_3$	In 3d	198143.20	27273.6691	0.20%	1.47	1.88%
	S 2p	26946.15	40338.5479			
	Zn 2p	754.5	134.997316			
2%Zn−In$_2$$_{-x}S_3$	In 3d	108815.68	14978.0713	0.46%	1.46	2.61%
	S 2p	14784.45	22132.4101			
	Zn 2p	966.9	173.000536			
3%Zn−In$_2$$_{-x}S_3$	In 3d	102982.85	14175.2035	1.08%	1.43	4.92%
	S 2p	13869.6	20762.8742			
	Zn 2p	2140.95	383.064949			
4%Zn−In$_2$$_{-x}S_3$	In 3d	116921.52	16093.8091	1.93%	1.38	8.27%
	S 2p	15503.7	23209.1317			
	Zn 2p	4327.5	774.288781			
5%Zn−In$_2$$_{-x}S_3$	In 3d	103702.52	14274.2630	2.31%	1.44	4.11%
	S 2p	14533.35	21756.5119			
	Zn 2p	4758.3	851.368760			

The calculation method for Vs concentrations:

Atomic concentration of Zn $= \dfrac{Area_{Zn}}{Area_{Zn} + Area_{In} + Area_S}$

$S/(In + Zn) = \dfrac{Area_S}{Area_{In} + Area_{Zn}}$ $Area$: Area(RSF*T*MFP) of corresponding elements

Vs concentrations[#] (%) $= \dfrac{S{:}In(In_2S_3) - S{:}(Zn + In)(xIn_{2-x}S_3)}{S{:}In(In_2S_3)}$

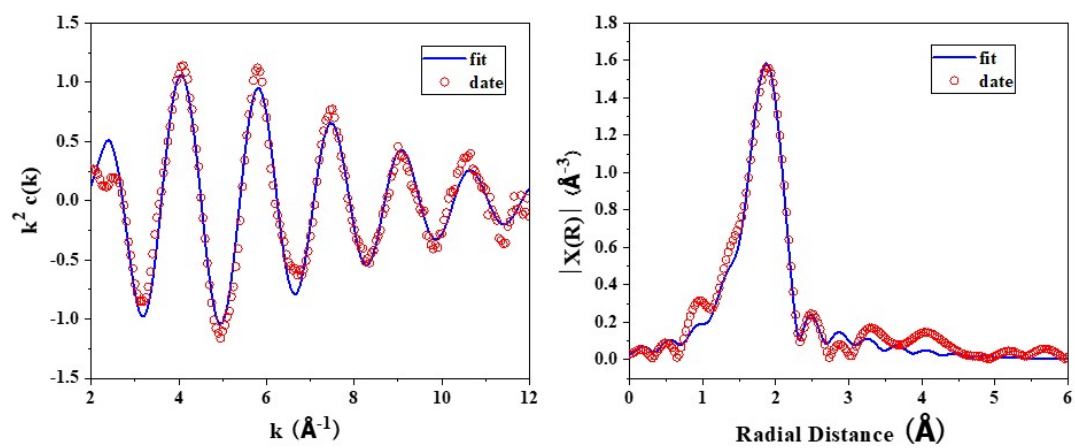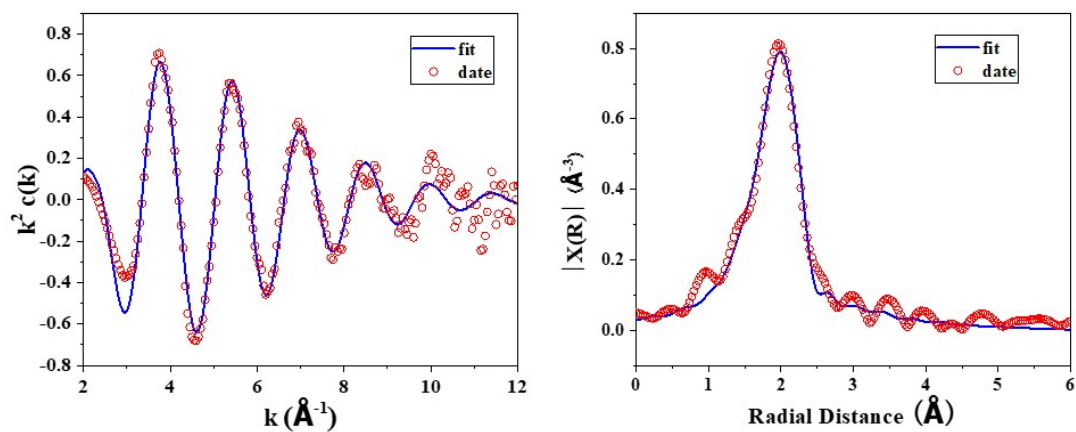**Fig. S10** Zn K-edge EXAFS fitting results of 4%Zn−In$_{2-x}$S$_3$.

Fig. S11 In L-edge EXAFS fitting results of In₂S₃.
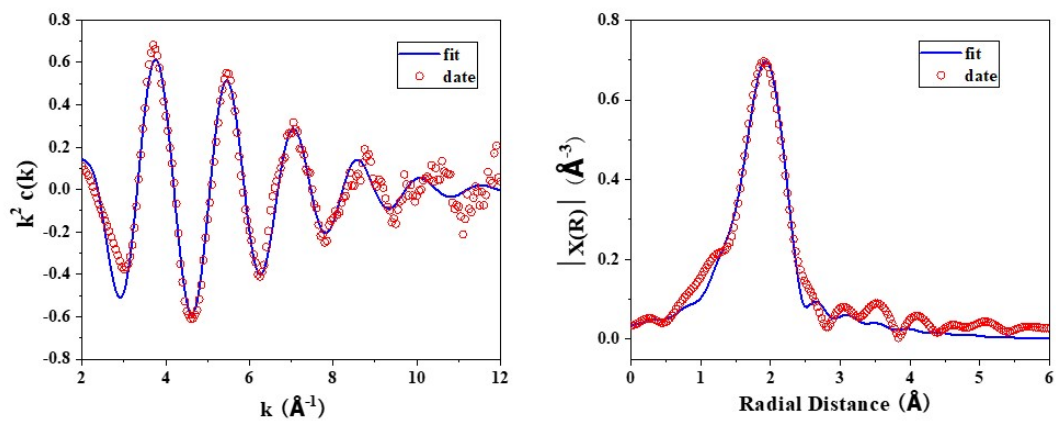
Fig. S12 In L-edge EXAFS fitting results of 4%Zn−In$_{2-x}$S$_3$.

Table S3. Fitting parameters for Zn K-edge and In L-edge EXAFS for the sample.

Sample	Shell	CN^a	$R(Å)^b$	$\sigma^2(Å^2)^c$	$\Delta E_0(eV)^d$	S_0^2	R factor
Zn foil	Zn-Zn	6 (set)	2.64	0.011	-0.9±0.5	0.8105 (calculated)	0.015
ZnS	Zn-S	4.2±0.2	2.34	0.006	4.2±0.5	0.8105(set)	0.017
4%Zn−In$_2$S$_3$	Zn-S	4.0±0.1	2.33	0.006	2.2±0.4	0.8105(set)	0.011
In foil	In-In	4 (set)	3.45	0.024	2.1±0.1	0.9024 (calculated)	0.003
	In-In2	8 (set)	3.22	0.022			
In$_2$S$_3$	In-S	5.8±0.2	2.55	0.013	1.6±0.3	0.9024(set)	0.015
4%Zn−In$_2$S$_3$	In-S	5.5±0.2	2.52	0.014	-0.8±0.3	0.9024(set)	0.015

[a]CN, coordination number; [b]R, the distance to the neighboring atom; [c]σ^2, the Mean Square Relative Displacement (MSRD); [d]ΔE_0, inner potential correction; R factor indicates the goodness of the fit. S_0^2 was fixed to 0.8081, according to the experimental EXAFS fit of the sample foil by fixing CN as the known crystallographic value. This value was fixed during EXAFS fitting, based on the known structure of In foil. Data ranges $3.0 \leq k \leq 10.0$ Å^{-1}, $1.0 \leq R \leq 3.0$ Å. The Debye-Waller factors and ΔRs are based on the *guessing* parameters and constrained for paths.
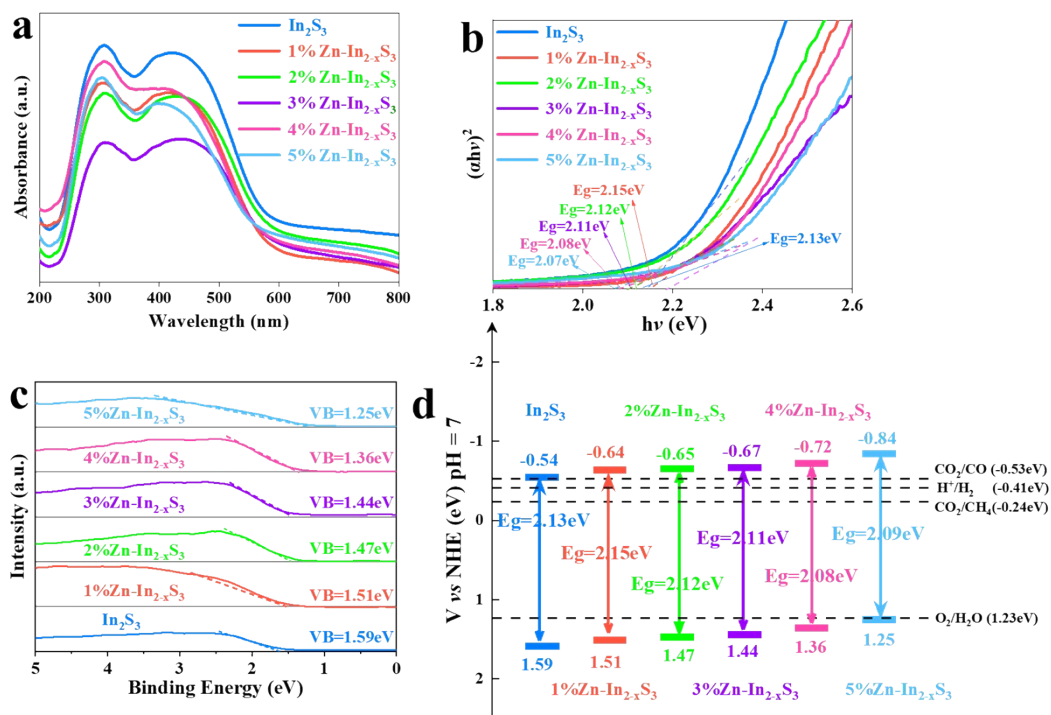
Fig. S13 (a) UV-*vis* DRS spectra, (b) (αhv)^2 versus (hv) plots, (c) Valence band spectra of X-ray photoelectron spectroscopy and (d) Band structures of In_2S_3 and xZn−$In_{2-x}S_3$ (x=1% ~ 5%).

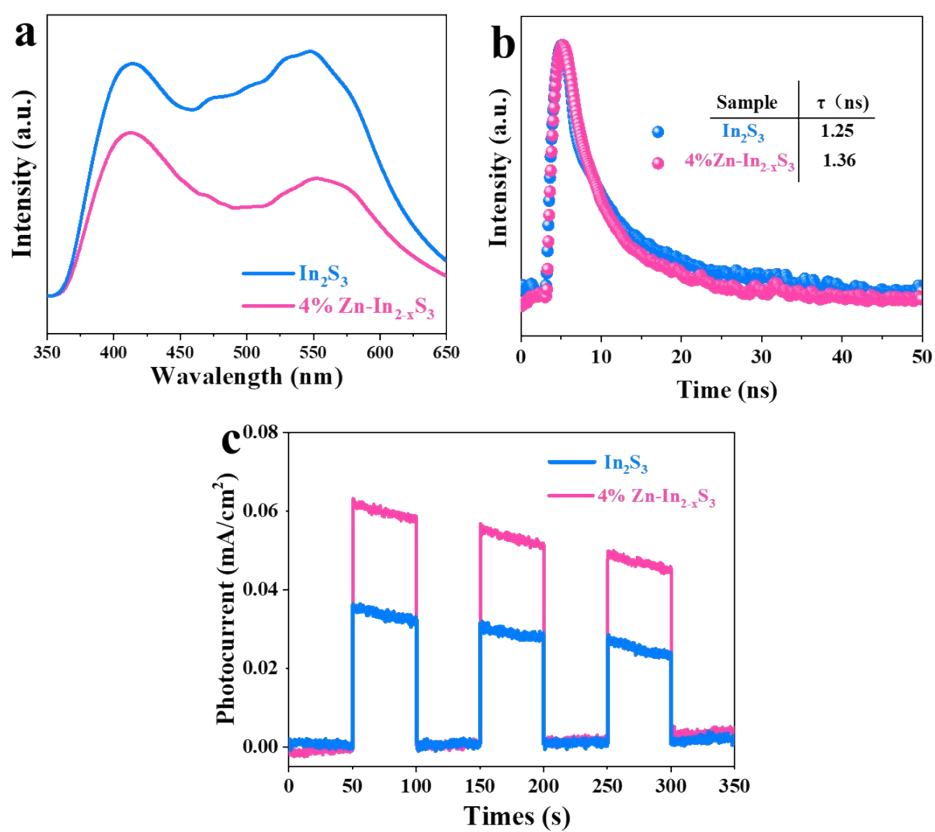**Fig. S14** (a) PL spectra, TRPL spectra and (c) Photocurrent response of In_2S_3 and $4\%Zn-In_{2-x}S_3$.

Table S4. The PL lifetime of In_2S_3 and 1-6%Zn−$In_{2-x}S_3$.

sample Parameters	In_2S_3	1%Zn-$In_{2-x}S_3$	2%Zn-$In_{2-x}S_3$	3%Zn-$In_{2-x}S_3$	4%Zn-$In_{2-x}S_3$	5%Zn-$In_{2-x}S_3$	6%Zn-$In_{2-x}S_3$
τ_1(ns)	0.2173	0.1983	0.3834	0.2262	0.2373	0.1986	0.2785
τ_2(ns)	1.4836	1.3141	1.2396	1.1497	1.0168	1.1726	1.9517
τ_3(ns)	7.2247	6.1418	7.7928	6.2869	7.5325	5.1024	11.4223
A_1	0.413	0.434	0.229	0.36	0.266	0.459	0.344
A_2	0.002	0.02	0.032	0.031	0.065	0.016	0.01
A_3	0.002	0.002	0.001	0.001	0.002	0.001	0
τ_A(ns)	1.25	1.01	1.06	0.80	1.36	0.58	0.56

[#] The calculated formula:

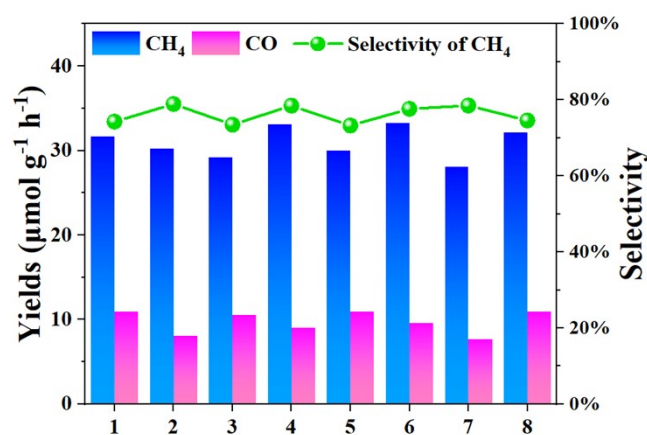$$\tau_A = \frac{A_1\tau_1^2 + A_2\tau_2^2 + A_3\tau_3^2}{A_1\tau_1 + A_2\tau_2 + A_3\tau_3}$$

Fig. S16 The CH$_4$ selectivity and the yields of CH$_4$ and CO over 4%Zn−In$_{2-x}$S$_3$ (1mg catalyst dispersed in 6 mL water), which were obtained from 8 parallel experiments.

Fig. S17 The CH_4 selectivity and the yields of CH_4 and CO over $4\%Zn-In_{2-x}S_3$ (2mg catalyst dispersed in 6 mL water), which were obtained from 8 parallel experiments.
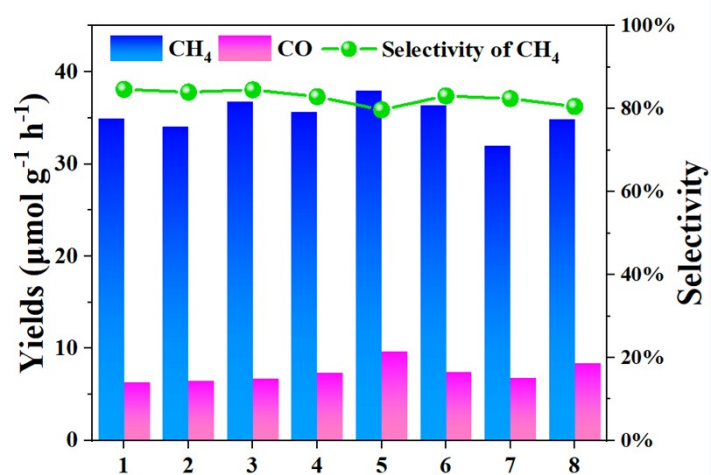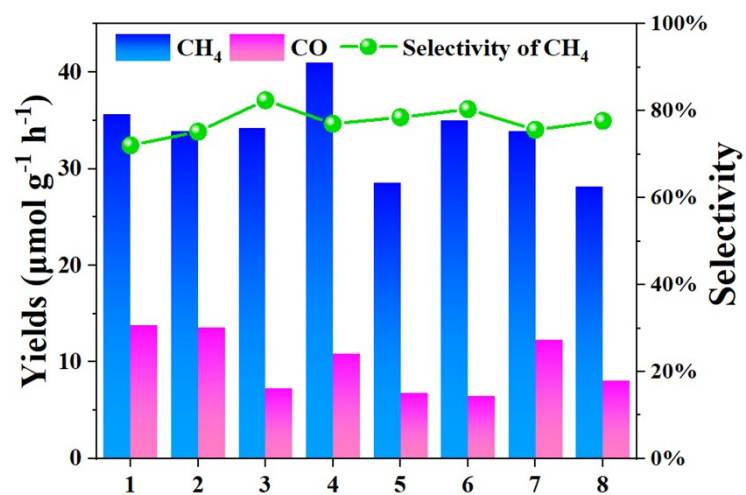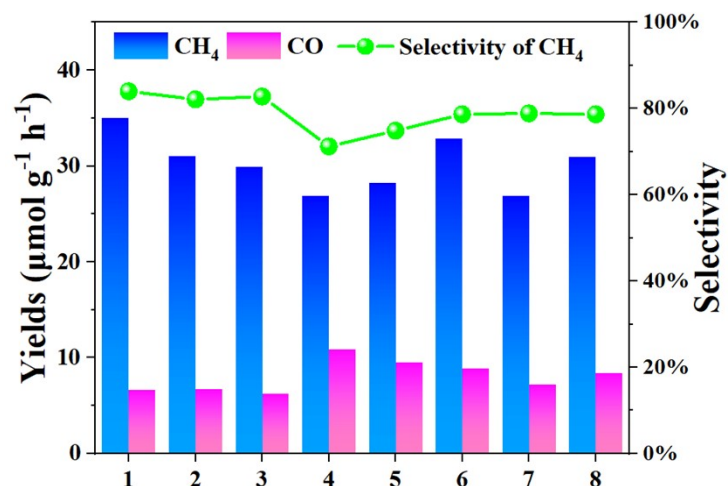
Fig. S18 The CH$_4$ selectivity and the yields of CH$_4$ and CO over 4%Zn−In$_{2-x}$S$_3$ (3mg catalyst dispersed in 6 mL water), which were obtained from 8 parallel experiments.

Fig. S19 The CH$_4$ selectivity and the yields of CH$_4$ and CO over 4%Zn−In$_{2-x}$S$_3$ (1mg catalyst dispersed in 6 mL water), which were obtained from 8 parallel experiments.

Table S5. The different partial pressure ratios of Ar/CO$_2$.

	CO$_2$ Volume	Ar Volume	partial pressure ratios of Ar/CO$_2$
1	50ml	5ml	0.1atm
2	50ml	10ml	0.2atm
3	50ml	15ml	0.3atm
4	50ml	20ml	0.4atm
5	50ml	25ml	0.5atm
6	50ml	30ml	0.6atm
7	50ml	36ml	0.7atm
8	50ml	40ml	0.8atm

Table S6. Performance comparison with other sulfur-based catalysts for photocatalytic CO_2 reduction reaction without sacrificial agents. (RT: Room Temperature)

Catalysts	Light source	Reaction medium	Products and yields	Selectivity of CH_4	Reference
4%Zn-In$_{2-x}$S$_3$	300 W Xe lamp (λ＞420nm)	H$_2$O(l), RT	CH$_4$(50.7μmol g^{-1}h^{-1}) CO (4.2μmol g^{-1}h^{-1})	92.3%	This work
MoS$_2$/In$_2$S$_3$	300 W Xe lamp (300＜λ＞700nm)	H$_2$O(l), RT	CH$_4$ (68.41μmol g^{-1}h^{-1}) CO (10.09μmol g^{-1}h^{-1}) CH$_3$OH (6.66μmol g^{-1}h^{-1})	80.3%	Ref.1
Fe/SiC	300 W Xe lamp (λ＞420nm)	Gas-solid, water, 298K	CH$_4$(28.3μmol g^{-1}h^{-1}) CO (1.7μmol g^{-1}h^{-1})	94.3%	Ref.2
UiO-66/Co$_9$S$_8$	300 W Xe lamp (AM 1.5G and cut 800 nm filter)	H$_2$O(l), RT	CH$_4$(25.7μmol g^{-1}h^{-1})	100%	Ref.3
CuSnInS$_4$	300 W Xe lamp (λ＞420nm)	Gas-solid, water, RT	CH$_4$ (5.83μmol g^{-1}h^{-1}) CO (2.4μmol g^{-1}h^{-1})	67.3%	Ref.4
1%Pt/CuInSnS$_4$	300 W Xe lamp (λ＞420nm)	Gas-solid, water, RT	CH$_4$ (43.25μmol g^{-1}h^{-1}) CO (7.85μmol g^{-1}h^{-1})	84.6%	Ref.4
10%CoO/CuInSnS$_4$	300 W Xe lamp (λ＞420nm)	Gas-solid, water, RT	CH$_4$ (33.3μmol g^{-1}h^{-1}) CO (9.36μmol g^{-1}h^{-1})	78.1%	Ref.4
10%NiO/CuInSnS$_4$	300 W Xe lamp (λ＞420nm)	Gas-solid, water, RT	CH$_4$ (11.8μmol g^{-1}h^{-1}) CO (6.85μmol g^{-1}h^{-1})	63.3%	Ref.4
5%Co(OH)$_2$ /CuInSnS$_4$	300 W Xe lamp (λ＞420nm)	Gas-solid, water, RT	CH$_4$ (145.45μmol g^{-1}h^{-1}) CO (32.32μmol g^{-1}h^{-1})	81.8%	Ref.4
5%Co(OH)$_2$ /CuInSnS$_4$/1%Pt	300 W Xe lamp (λ＞420nm)	Gas-solid, water, RT	CH$_4$ (195.6μmol g^{-1}h^{-1}) CO (22.0μmol g^{-1}h^{-1})	89.9%	Ref.4
CuS@ZnIn$_2$S$_4$/ C60	300 W Xe lamp (λ＞400nm)	Gas-solid, water, 25℃	CH$_4$ (43.6μmol g^{-1}h^{-1}) CO (6.4μmol g^{-1}h^{-1})	87.2%	Ref.5
Pd$_{1+NPs}$/C$_3$N$_4$	Xe lamp (250mW cm^{-2})	H$_2$O(l), RT	CH$_4$ (20.3μmol g^{-1}h^{-1}) CO (0.46μmol g^{-1}h^{-1})	97.8%	Ref.6
black Nb$_2$O$_{5-x}$NFs	300 W Xe lamp (λ＞420nm)	H$_2$O(l), RT	CH$_4$ (19.5μmol g^{-1}h^{-1}) CO (10.6μmol g^{-1}h^{-1})	64.8%	Ref.7
Au$_{SA}$/Cd$_{1-x}$S	300 W Xe lamp (UV-vis)	Gas-solid, water, RT	CH$_4$ (11.3μmol g^{-1}h^{-1}) CO (32.2μmol g^{-1}h^{-1})	22.0%	Ref.8
Au$_{SA}$/CdS$_{1-x}$	300 W Xe lamp (UV-vis)	Gas-solid, water, RT	CH$_4$ (0.40μmol g^{-1}h^{-1}) CO (3.70μmol g^{-1}h^{-1})	9.3%	Ref.8
Ni-doped CoS$_2$ nanosheets	300 W Xe lamp (AM 1.5G and cut	Gas-solid, water, RT	CH$_4$ (101.8μmol g^{-1}h^{-1})	~73.1%	Ref.9

	800 nm filter)		CO (37.5μmol g^{-1}h^{-1})		
Ag$_2$S-In$_2$S$_3$	300 W Xe lamp (AM 1.5G)	Gas-solid, water, 298K	CH$_4$ (20μmol g^{-1}h^{-1}) CO (25.1μmol g^{-1}h^{-1})	44.3%	Ref.10
In$_4$SnS$_8$	300 W Xe lamp (λ＞420nm)	Gas-solid, water, RT	CH$_4$ (23.88μmol g^{-1}h^{-1}) CO (20.96μmol g^{-1}h^{-1})	57.0%	Ref.11
TiO$_2$@ZnIn$_2$S$_4$	300 W Xe lamp	Gas-solid, water, RT	CH$_4$ (4.26μmol g^{-1}h^{-1}) CO (9.28μmol g^{-1}h^{-1}) CH$_3$OH (4.78μmol g^{-1}h^{-1})	23.3%	Ref.12
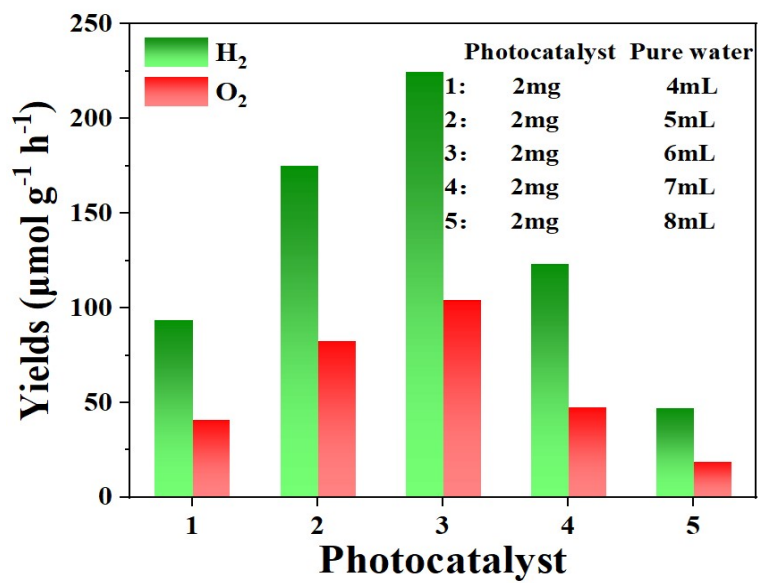
Fig. S20 The effect of dispersion concentrations of photocatalyst on photocatalytic performance of water splitting of 4% Zn−$In_{2-x}S_3$ (photocatalyst: 2mg, H_2O: in 4 ～ 8mL).
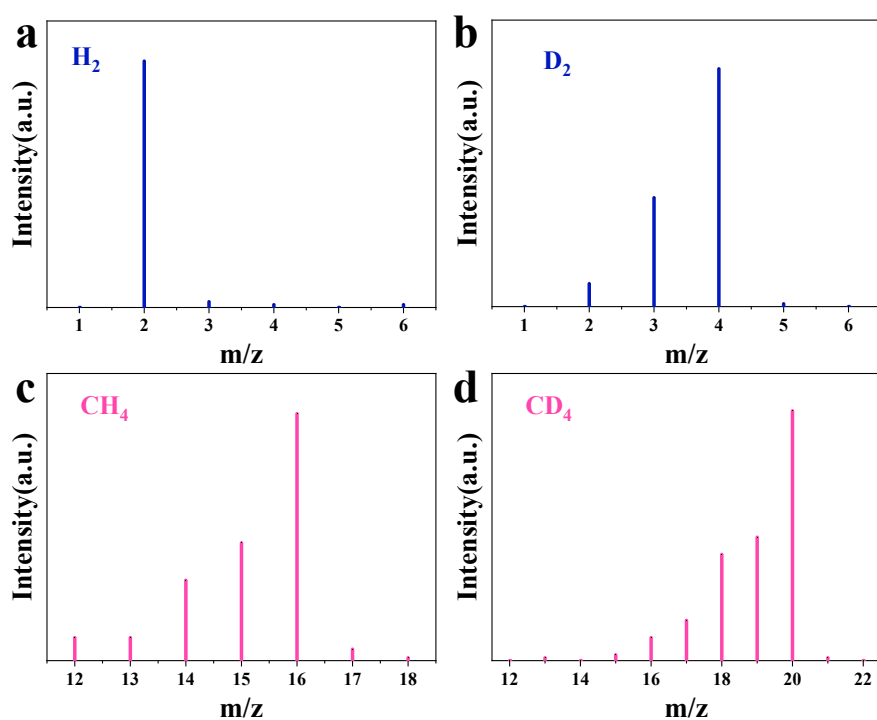
Fig. S21 Mass spectra of (a) H_2 (m/z=2) and (b) D_2 (m/z=4) produced by 4%Zn−$In_{2-x}S_3$ photocatalysts during the water splitting reaction when H_2O and D_2O are used as proton sources, respectively. Mass spectra of (c) CH_4 and (d) CD_4 produced by 4%Zn−$In_{2-x}S_3$ photocatalyst during CO_2 reduction reaction using H_2O and D_2O as proton sources, respectively.
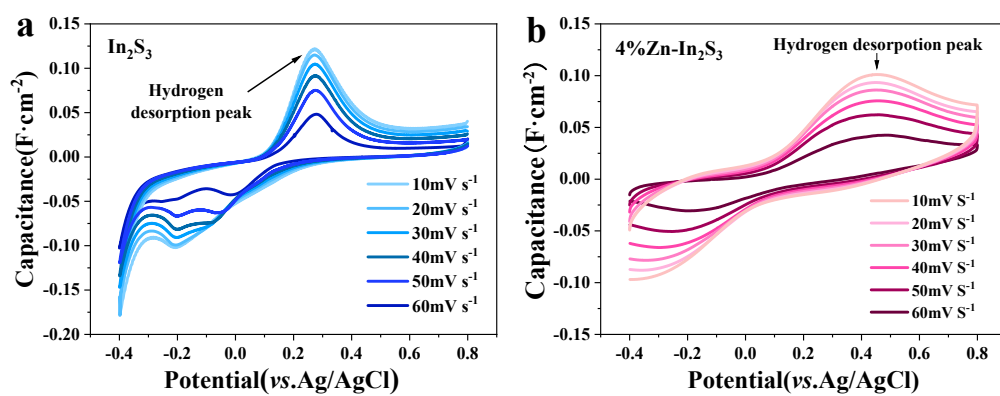
Fig. S22 Cyclic voltammetry of (a) In_2S_3 and (b) $4\%Zn-In_{2-x}S_3$ in Ar-saturated 0.5M H_2SO_4 with a scan rate of 10~60mV s^{-1}.

Table S7. Intermediate product processes of H_2O adsorption and activation, and CO_2 hydrogenation and conversion over In_2S_3.
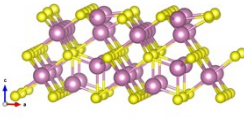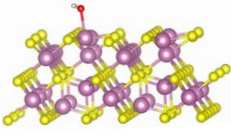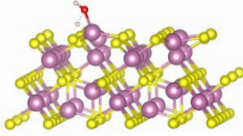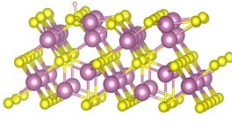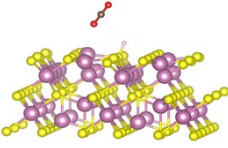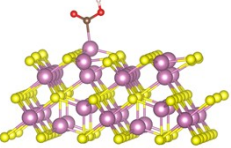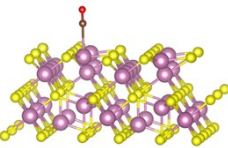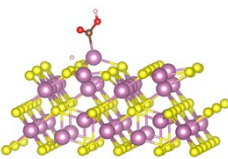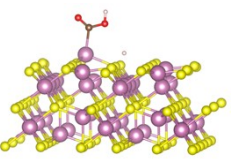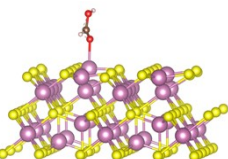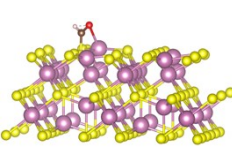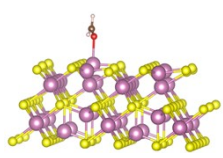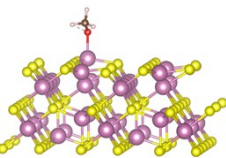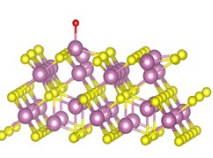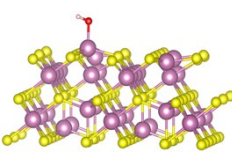
In_2S_3	*+H_2O	*H_2O	*H
*H + CO_2	*COOH	*CO	
*COOH-Ha	*COOH-Hb	*CHOOH	*CHO
*CH_2O	*CH_3O	*O	*OH

Table S8. Intermediate product processes of H_2O adsorption and activation, and CO_2 hydrogenation and conversion over 4%Zn-$In_{2-x}S_3$
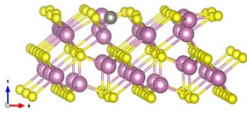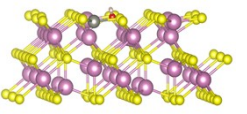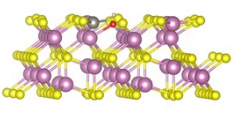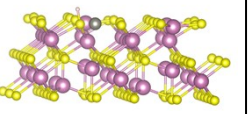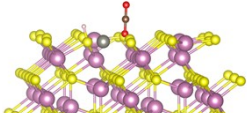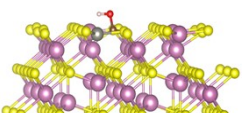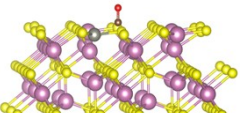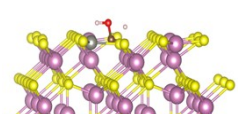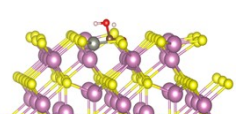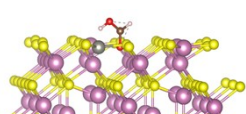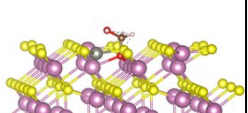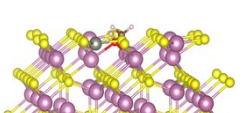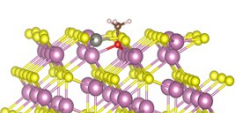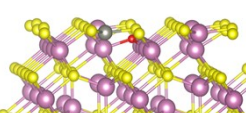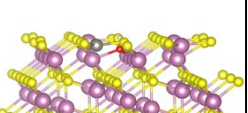
4% Zn−$In_{2-x}S_3$	*+H_2O	*H_2O	*H
*H + CO_2	*COOH	*CO	
*COOH-Ha	*COOH-Hb	*CHOOH	*CH_2OOH
*CH_2O	*CH_3O	*O	*OH

Fig. S23 The infrared thermal images of different photocatalyst sample with increasing irradiation time (0 ~ 3 min). (20 mg photocatalyst, 300W Xenon lamps, λ>420 nm, the distance between powders and light: 10 cm)

Photocatalyst \ Irradiation times	0 min	1 min	3 mins
In_2S_3			
1%$Zn-In_{2-x}S_3$			
2%$Zn-In_{2-x}S_3$			
3%$Zn-In_{2-x}S_3$			
4%$Zn-In_{2-x}S_3$			
5%$Zn-In_{2-x}S_3$			
6%$Zn-In_{2-x}S_3$			
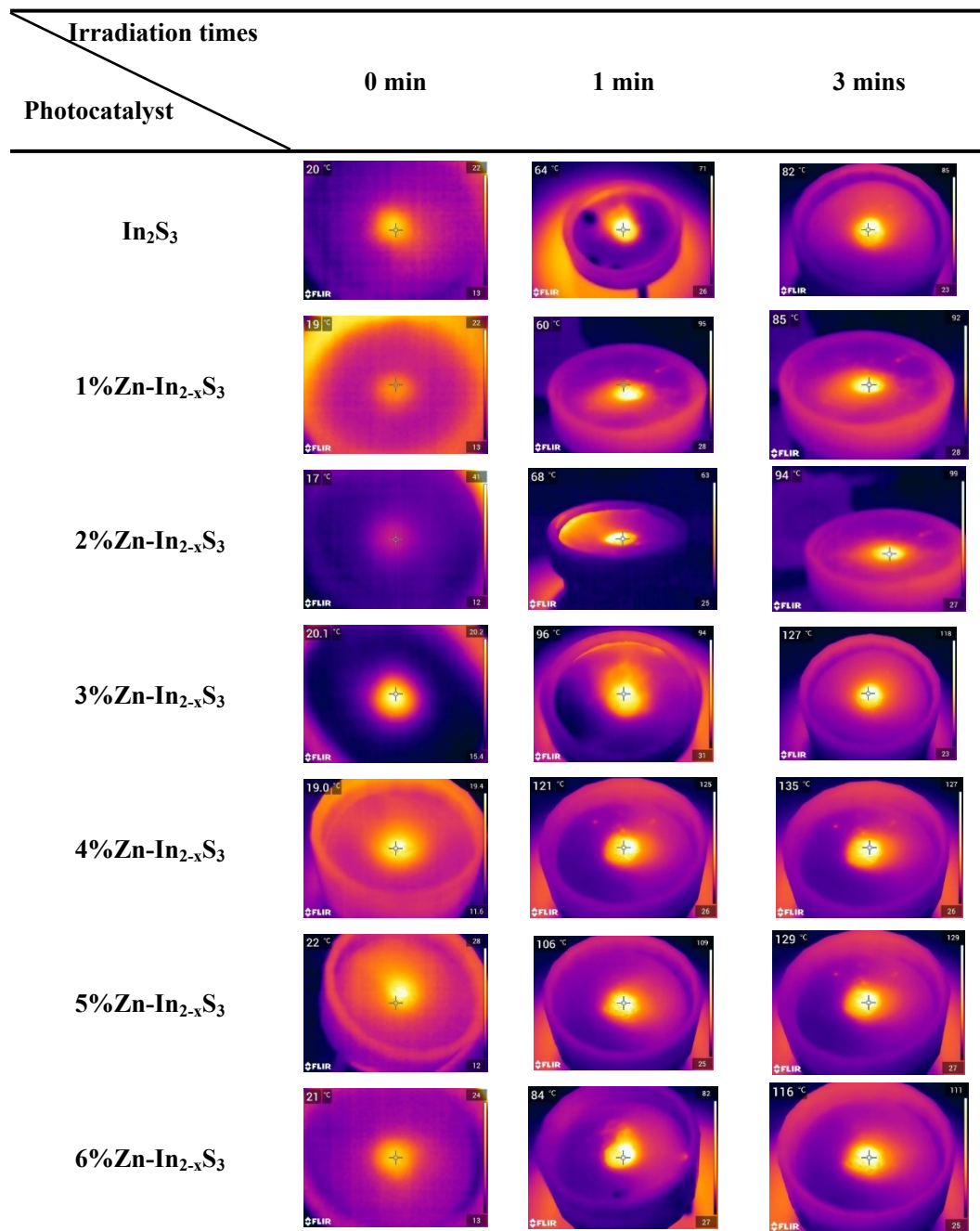
References

[1] Cai, W.; Qian, Z.; Hu, C.; Zheng, W.; Luo, L.; Zhao, Y. Systematic investigation of MoS_2-metal sulfides (Metal = In, Sn, Cu, Cd) heterostructure via metal-sulfur bond for photocatalytic CO_2 reduction. *Chem. Eng. J.* 2024, 479, 147718.

[2] Lin, Q.; Zhao, J.; Zhang, P.; Wang, S.; Wang, Y.; Zhang, Z.; Wen, N.; Ding, Z.; Yuan, R.; Wang, X.; Long, J. Highly selective photocatalytic reduction of CO_2 to CH_4 on electron-rich Fe species cocatalyst under visible light irradiation. *Carbon Energy*, 2024, 6, e435.

[3] Yang, S.; Byun, W. J.; Zhao, F.; Chen, D.; Mao, J.; Zhang, W.; Peng, J.; Liu, C.; Pan, Y.; Hu, J.; Zhu, J.; Zheng, X.; Fu, H.; Yuan, M.; Chen, H.; Li, R.; Zhou, M.; Che, W.; Back, J. B.; Lee, J. S.; Xu, J. CO_2 enrichment boosts highly selective infrared-light-driven CO_2 conversion to CH_4 by UiO-66/Co_9S_8 photocatalyst. *Adv. Mater.* 2024, 36, 2312616.

[4] Chai, Y.; Kong, Y.; Lin, M.; Lin, W.; Shen, J.; Long, J.; Yuan, R.; Dai, W.; Wang, X.; Zhang, Z. Metal to non-metal sites of metallic sulfides switching products from CO to CH_4 for photocatalytic CO_2 reduction. *Nat. Commun.* 2023, 14, 6168.

[5] Ding, Y.; Chen, Y.; Guan, Z.; Zhao, Y.; Lin, J.; Jiao, Y.; Tian, G. Hierarchical CuS@$ZnIn_2S_4$ hollow double-shelled p–n heterojunction octahedra decorated with fullerene C60 for remarkable selectivity and activity of CO_2 photoreduction into CH_4. *ACS Appl. Mater. Interfaces* 2022, 14, 7888–7899.

[6] Liu, P.; Huang, Z.; Gao, X.; Hong, X.; Zhu, J.; Wang, G.; Wu, Y.; Zeng, J.; Zheng, X. Synergy between palladium single atoms and nanoparticles via hydrogen spillover for enhancing CO_2 photoreduction to CH_4. *Adv. Mater.* 2022, 34, 2200057.

[7] Lin, X.; Xia, S.; Zhang, L.; Zhang, Y.; Sun, S.; Chen, Y.; Chen, S.; Ding, B.; Yu, J.; Yan, J. Fabrication of flexible mesoporous black Nb_2O_5 nanofiber films for visible-light-driven photocatalytic CO_2 reduction into CH_4. *Adv. Mater.* 2022, 34, 2200756.

[8] Cao, Y.; Guo, L.; Dan, M.; Doronkin D. E.; Han, C.; Rao, Z.; Liu, Y.; Meng, J.; Huang, Z.; Zheng, K.; Chen, P.; Dong, F.; Zhou, Y. Modulating electron density of vacancy site by single Au atom for effective CO_2 photoreduction. *Nat. commun.* 2021, 12, 1675.

[9] Xu, J.; Ju, Z.; Zhang, W.; Pan, Y.; Zhu, J.; Mao, J.; Zheng, X.; Fu, H.; Yuan, M.; Chen, H.; Li, R. Efficient infrared-light-driven CO_2 reduction over ultrathin metallic Ni-doped CoS_2 nanosheets. *Angew. Chem. Int. Ed.* 2021, 133, 8787–8791.

[10] Shao, W.; Wang, S.; Zhu, J.; Li, X.; Jiao, X.; Pan, Y.; Sun, Y.; Xie, Y. In-plane heterostructured Ag_2S-In_2S_3 atomic layers enabling boosted CO_2 photoreduction into CH_4. *Nano Res.* 2021, 14, 4520–4527.

[11] Chai, Y.; Chen, Y.; Shen, J.; Ni, M.; Wang, B.; Li, D.; Zhang, Z.; Wang, X. Distortion of the coordination structure and high symmetry of the crystal structure in In_4SnS_8 microflowers for enhancing visible-light photocatalytic CO_2 reduction. ACS Catal. 2021, 11, 11029–11039.

[12] Wang, L.; Cheng, B.; Zhang, L.; Yu, J. In situ irradiated XPS investigation on S-scheme TiO_2@$ZnIn_2S_4$ photocatalyst for efficient photocatalytic CO_2 reduction. *Small* 2021, 17, 2103447.